Magic numbers, excitation levels, and other properties of small neutral ^{4}He clusters ($N \leq 50$)

Rafael Guardiola
Departamento de Física Atómica y Nuclear, Facultad de Fisica, Universidad de Valencia, 46100 Burjassot, Spain

Oleg Kornilov
Max-Planck-Institut fur Dynamik und Selbstorganisation, Bunsenstrasse 10, 37073 Gottingen, Germany

Jesús Navarro[a)]
IFIC (CSIC-Universidad de Valencia), Apartado 22085, 46071 Valencia, Spain

J. Peter Toennies
Max-Planck-Institut fur Dynamik und Selbstorganisation, Bunsenstrasse 10, 37073 Gottingen, Germany

The ground-state energies and the radial and pair distribution functions of neutral ^{4}He clusters are systematically calculated by the diffusion Monte Carlo method in steps of one ^{4}He atom from 3 to 50 atoms. In addition the chemical potential and the low-lying excitation levels of each cluster are determined with high precision. These calculations reveal that the "magic numbers" observed in experimental ^{4}He cluster size distributions, measured for free jet gas expansions by nondestructive matter-wave diffraction, are not caused by enhanced stabilities. Instead they are explained in terms of an enhanced growth due to sharp peaks in the equilibrium concentrations in the early part of the expansion. These peaks appear at cluster sizes which can just accommodate one more additional stable excitation. The good agreement with experiment provides not only experimental confirmation of the energy level and the chemical potential calculations, but also evidence for a new mechanism which can lead to magic numbers in cluster size distributions. By accounting for the falloff of the radial density distributions at the surface and a size-dependent surface tension, the energy levels are demonstrated to be consistent with a modified Rayleigh model of surface excitations. The compressibility coefficient of these small clusters is found to be one order of magnitude smaller than the bulk compressibility. © *2006 American Institute of Physics*. [DOI: 10.1063/1.2140723]

I. INTRODUCTION

Finite-sized helium clusters and droplets have recently attracted considerable attention both from experimentalists[1,2] and theoreticians.[2–4] This revival of interest is largely motivated by the recent discovery that droplets with more than 10^3 ^{4}He atoms are ideally gentle and extremely cold cryomatrices both for high-resolution spectroscopy as well as for synthesizing new molecular species and clusters.[1] At the same time, the spectroscopic information gained reveals new manifestations of superfluidity on a molecular level.[1,5] Since in small ^{4}He clusters with less than about 50 atoms the chromophores have a much larger perturbing effect on the properties of the surrounding helium atoms[6] the spectral information in this case is usually largely dominated by the chromophore interactions. Thus for small *pure* helium clusters most of the available data on the ground-state properties stem from computations based on Green's-function Monte Carlo,[7] diffusion Monte Carlo (DMC),[8–10] or Feynman's path-integral Monte Carlo techniques.[11] Since the helium-helium interaction potential is now well known[12] these techniques can be expected to provide essentially exact information.

One question about ^{4}He clusters which has been frequently discussed in the literature since the earliest calculations[13] is the possible existence of magic numbers, which are usually associated with particularly energetically stable configurations of clusters with a certain number of atoms. It is now well known, for instance, that van der Waals clusters of the heavy rare gases, such as Xe and Kr, manifest an enhanced ground-state stability for number sizes 13, 55, and 147, which are interpreted in terms of favorable icosahedral geometrical packings of classical spheres.[14] As opposed to all other clusters helium clusters are, however, definitely liquid, so that well-defined structures are not expected.[13] The present theoretical calculations confirm earlier results indicating a smooth behavior of both the ground-state energies and the chemical potentials, i.e., single-particle evaporation energies, with the number size and rule out magic numbers related to particularly enhanced stabilities.

Thus it came somewhat of a surprise when recently the number size distributions in a beam of neutral ^{4}He clusters produced in a free jet gas expansion were measured[15] by the nondestructive technique of matter diffraction from a 100 nm period transmission grating. Instead of the expected smooth distribution, distinct peaks at $N=10$ and 11, 14, 22, 26 and 27, and 44 atoms were observed. In a previous brief commu-

---
[a)]Electronic mail: navarro@ific.uv.es

nication by the present authors[15] each of these "magic numbers" was interpreted as the threshold size for which an additional quantized excitation level, calculated with the DMC method, is stabilized as its energy drops below the chemical potential. Indeed, in the early formative stages of the gas expansions, where quasiequilibrium still holds, the opening of an additional quantum state leads to a jump in the partition function of the affected cluster and can explain the observations.

The quantized collective excited states have, in the past, also been studied within several theoretical approaches,[8,16–19] which reveal that helium clusters can sustain collective oscillations of different multipolarities. The behavior of the maxon-roton excitation spectrum as a function of the number of constituents obtained in these calculations has been used[16] to establish the onset of superfluidity in small ^{4}He clusters. Evidence for the maxon-roton excitation was later observed spectroscopically in large droplets ($N \geqslant 10^3$ atoms) doped with an appropriate chromophore molecule.[20] Additional spectroscopic evidence for superfluidity in small clusters was based on the new phenomenon of free rotations, found to occur for OCS molecules surrounded by 60 ^{4}He atoms, the entire ^{4}He cluster being inside a larger ^{3}He droplet.[21] This limit has been pushed down to even smaller clusters with only about 6–10 ^{4}He atoms attached to various chromophores such as OCS, N_2O, and CO_2.[6,22,23] Up to recently, however, experimental data on the physical properties including the energy levels of small pure ^{4}He clusters ($N \leqslant 10^2$ atoms) have been completely lacking. Moreover, all the past calculations have been limited to arbitrarily chosen cluster sizes so that the changes in pure cluster excitation levels with the size N could not be traced out.

The purpose of the present paper is to provide a microscopic and accurate theoretical description of the ground state as well as the excited levels of pure ^{4}He clusters which resulted out of the initial and final analyses of the diffraction experiments.[15] The procedure is to solve the Schrödinger equation for a system of N ^{4}He atoms, interacting through the HFD-B(HE) two-body potential,[24] which is a compromise between *ab initio* calculations and phenomenological fits. Moreover, the sensitivity of the results on the interaction potential has been checked by also employing the more recent potentials LM2M2 (Ref. [25]) and TTY.[26] The Schrödinger equation has been solved by means of stochastic DMC techniques. The calculations have been carried out to a higher level of accuracy than in previous studies in order to have sufficient precision for a reliable comparison with the experimental phenomena. In addition to the excitation levels, the ground-state binding energies, chemical potentials, the radial density distributions, and the pair distribution functions have been calculated for all sizes from $N=3$ up to $N=50$ for the first time. It is found that the excitation levels deviate considerably from those predicted by the conventional liquid-drop model. The deviations can be explained by the width of the outer surface density falloff region and the size dependence of the surface tension.[27]

This article is organized as follows. In Sec. II, the technical details of the DMC calculations are discussed for the ground state and low-lying excited states. The results are presented and discussed in Sec. III. In Sec. IV the experiment and the analysis in terms of the abundances in the free jet expansions of helium clusters are described in more detail than in Ref. [15]. An equilibrium model is introduced, which facilitates the calculation of the magic numbers from the excitation energies. In Sec. V calculated one- and two-body distribution functions are presented. In Sec. VI, the excitation energies are shown to be consistent with the liquid-drop model if the radial distribution functions are taken into account. This makes it possible to deduce the size dependence of the surface tension. The article closes with a summary and an outlook for new challenges.

II. THE DIFFUSION MONTE CARLO METHOD

In DMC method[28] the imaginary-time Schrödinger equation is solved for a function $f(\mathcal{R}, t) = \Phi_{var}(\mathcal{R})\Psi(\mathcal{R}, t)$ which is the product of the importance-sampling wave function Φ_{var} and the true ground-state wave function Ψ. The variable $\mathcal{R}$ represents the set $(\mathbf{r}_1, \ldots, \mathbf{r}_N)$ of $3N$ coordinates of the N atoms which form the drop. The solution for f is obtained by constructing an approximate small-time Green's function $G(\mathcal{R}, \mathcal{R}', \tau)$ which serves to advance f by a small time step τ,

$$f(\mathcal{R}', t + \tau) = \int d\mathcal{R} \, G(\mathcal{R}', \mathcal{R}, \tau) f(\mathcal{R}, t). \tag{1}$$

The $O(\tau^3)$ time-dependent Green's function,

$$\begin{aligned} G(\mathcal{R}, \mathcal{R}', \tau) = \frac{1}{(4\pi D\tau)^{3N/2}} &\exp\{-\tau[(E_L(\mathcal{R}) + E_L(\mathcal{R}'))/2 \\ &- E]\} \times \exp\{-[\mathcal{R}' - \mathcal{R} - D\tau(F(\mathcal{R}) \\ &+ F(\mathcal{R}'))/2]^2/4D\tau\}, \end{aligned} \tag{2}$$

was used, as described in Refs. [29] and [30] since it provides an accurate and economical method for the small-time iterative procedure. In Eq. (2), $D = \hbar^2/2m$ is an effective diffusion constant, where m is the ^{4}He atomic mass, $F(\mathcal{R}) = 2\nabla \ln \Phi_{var}(\mathcal{R})$ is the drift force or drift velocity, and $E_L(\mathcal{R}) = \Phi_{var}^{-1}(\mathcal{R})H\Phi_{var}(\mathcal{R})$ is the local energy. The energy shift E in the first exponential appearing on the right-hand side of Eq. (2) controls the normalization of the function f.

The Monte Carlo solution of the differential equation consists in creating a set of walkers $\{\mathcal{R}_1, \mathcal{R}_2, \ldots, \mathcal{R}_{N_w}\}$ to represent the function $f(\mathcal{R}, 0)$ at the initial time and applying successively the short-time approximate Green's function a large number of times. In practice, this means that a new set of walkers is obtained from the previous one by applying the operations of isotropic diffusion, drift, and replication, implicit in the short-time approximated Green's function of Eq. (2), as well as by adjusting the energy shift E to maintain a stable population. The specific form for carrying out such transformations may be found in Ref. [29]. After many repeated applications all components of the starting wave function orthogonal to the ground-state wave function disappear, and the contributions of the other eigenstates go exponentially to zero as the time goes to infinity. The remaining set of walkers then provides a valid representation of the quantity,

$$f(\mathcal{R}, t \to \infty) \to \Phi_{\mathrm{var}}(\mathcal{R})\Psi(\mathcal{R}), \tag{3}$$

i.e., the product of the exact ground-state wave function and the driving starting wave function Φ_{var}. From this converged product the mixed estimators of physically interesting quantities, such as the total energy, can be computed

$$E_{\mathrm{tot}} = \frac{\int f(\mathcal{R}, t \to \infty) E_L(\mathcal{R}) d\mathcal{R}}{\int f(\mathcal{R}, t \to \infty) d\mathcal{R}}. \tag{4}$$

In order to have a good statistical accuracy it is convenient to continue the application of Green's function along a very large number of time steps and accumulate the resulting sets of walkers. Of course, since the walkers are strongly correlated a block average is carried out in order to estimate the statistical error.

A. Lowest $L \neq 0$ excited states

The ground state of a system of bosonic particles will have zero angular momentum, $L=0$, and therefore can be constructed by the proper choice of the importance-sampling wave function. At each iteration, the solution of the time-dependent Schrödinger equation is a mixture of the zero angular momentum eigenstates of the Hamiltonian. As discussed above, the iterated application of the DMC procedure selects the lowest eigenstate, i.e., the ground-state energy.

Importance-sampling wave functions with a nonzero angular momentum may equally well be considered, and correspondingly the initial state will be an admixture of eigenstates of a specified angular momentum L. Again, the application of the imaginary-time Green's function will select the lowest eigenstate in the subspace of angular momentum L, the remaining contributions being exponentially suppressed as the time increases. Certainly, this "ground state of subspace L" is not a positive definite function, and cannot be interpreted as a probability distribution function. However, once it is multiplied by the appropriate importance-sampling wave function it may correspond to a positive definite quantity, provided that the nodal surfaces of the importance-sampling wave function are the correct ones. This may not be guaranteed in advance, but this approach can still lead to valid results if the time-dependent random walk is restricted to movements that do not cross the nodal surfaces. This is the so-called fixed-node approximation,[31] largely used when dealing with fermionic systems. In the fixed-node approximation an exact energy for the lowest angular momentum L state is, in fact, not obtained. The improved variational wave function and the corresponding mixed estimator of the energy, which is derived, does, however, provide a variational upper bound.

A simple form of constructing an importance-sampling wave function with angular momentum L is to multiply the $L=0$ variational state $\Phi_{\mathrm{var}}(\mathcal{R})$ with an angular momentum L function

$$\Phi_{\mathrm{var}}^{(L)}(\mathcal{R}) = \left\{ \sum_{i=1}^{N} |\mathbf{r}_i - \mathbf{R}_{\mathrm{cm}}|^L P_L(\cos \bar{\theta}_i) \right\} \Phi_{\mathrm{var}}(\mathcal{R}), \tag{5}$$

where $\bar{\theta}_i$ is the azimuthal angle of the vector $\mathbf{r}_i - \mathbf{R}_{\mathrm{cm}}$ which defines the position of the ith particle with respect to the center-of-mass coordinate $\mathbf{R}_{\mathrm{cm}} = \Sigma_i \mathbf{r}_i / N$, and P_L is the Legendre polynomial. The form of this family of importance-sampling functions is simpler than it seems, because the factor carrying the angular momentum corresponds actually to the sum of harmonic polynomials of degree L in the variables $\mathbf{r}_i - \mathbf{R}_{\mathrm{cm}}$. Note that the sum over all the constituent particles is required to maintain the Bose symmetry, and the subtraction of the center-of-mass coordinate $\mathbf{R}_{\mathrm{cm}}$ is required to maintain the translational invariance.

This simple recipe holds for all L with the exception of $L=1$. In this case the factor entering the importance-sampling function is identically zero:

$$\sum_{i=1}^{N} |\mathbf{r}_i - \mathbf{R}_{\mathrm{cm}}| P_1(\cos \bar{\theta}_i) \equiv \sum_i (z_i - Z_{\mathrm{cm}}) = 0.$$

To overcome this difficulty, a different function of the radial distance to the center-of-mass is used for the $L=1$ calculation. The following function

$$\Phi_{\mathrm{var}}^{(1)}(\mathcal{R}) = \sum_{i=1}^{N} |\mathbf{r}_i - \mathbf{R}_{\mathrm{cm}}|^3 P_1(\cos \bar{\theta}_i) \Phi_{\mathrm{var}}(\mathcal{R}), \tag{6}$$

was found to be especially expedient from the computational point of view, but any other form would be equally acceptable. The only requirement is that the initial wave function has a non-null overlap with the exact lowest-energy wave function with angular momentum L. The DMC process will suppress, at long enough times, all higher-energy components.

B. Vibrational excitations

Besides the excited states with angular momentum L, one should also consider vibrational excitations characterized by a radial quantum number n. In short, each of the excited states will be represented by (n, L). The procedure explained in the previous subsection was used to obtain the exact energy of the ground state $(0,0)$ and an upper bound to the lowest energy of each subspace $(0, L)$. A useful estimate of the energies of the average vibrational excitations ($n \geqslant 1, L$) in each L subspace is obtained by using sum rules,[32,33] which only require the knowledge of the lowest L-state wave functions.

Consider the exact lowest state for a given angular momentum L and the full set of eigenstates of this subspace in order of increasing energy, represented by $\Psi_0^{(L)}$ and $\{\Psi_n^{(L)}, E_n^{(L)}\}$, respectively, where $n=0, 1,\ldots$, is the vibrational quantum number. Let $Q(\mathcal{R})$ be an arbitrary Hermitian operator, assumed to be scalar under rotations, for which the sum rule of order p is given by

$$M_p^{(L)}[Q] = \sum_{(n,\ell)\neq(0,L)} (E_n^{(\ell)} - E_0^{(L)})^p |\langle\Psi_n^{(\ell)}|Q|\Psi_0^{(L)}\rangle|^2, \qquad (7)$$

where $E_n^{(\ell)}$ is the energy of the state (n,ℓ), and the sum extends over all eigenstates of the Hamiltonian with the exception of the lowest-energy state $(0, L)$ of angular momentum L. Because of the assumed properties of Q only states with angular momentum $\ell=L$ will contribute to the sum. As $M_p^{(L)}$ is a sum of positive terms, the $p=1$ sum rule fulfills the property

$$M_1^{(L)}[Q] \equiv \sum_{n\neq 0} (E_n^{(L)} - E_0^{(L)})|\langle\Psi_n^{(L)}|Q|\Psi_0^{(L)}\rangle|^2$$
$$\geqslant (E_1^{(L)} - E_0^{(L)})M_0^{(L)}[Q], \qquad (8)$$

from which an upper bound to the energy of the first excited state of the subspace L is obtained,

$$E_1^{(L)} - E_0^{(L)} \leqslant \frac{M_1^{(L)}[Q]}{M_0^{(L)}[Q]}. \qquad (9)$$

The evaluation of the sum rules is simpler than it seems because of the relations[32,33]

$$M_0^{(L)}[Q] = \langle\Psi_0^{(L)}|Q^2|\Psi_0^{(L)}\rangle - |\langle\Psi_0^{(L)}|Q|\Psi_0^{(L)}\rangle|^2, \qquad (10)$$

$$M_1^{(L)}[Q] = \tfrac{1}{2}\langle\Psi_0^{(L)}|[Q,[H,Q]]|\Psi_0^{(L)}\rangle, \qquad (11)$$

which are easily obtained by using the completeness relation of the set of functions $\{\Psi_n^{(L)}\}$. The double commutator in Eq. (11) can be further simplified as the only contribution comes from the kinetic-energy operator

$$M_1^{(L)} = \frac{\hbar^2}{2m}\langle\Psi_0^{(L)}|\sum_{i=1}^N |\nabla_i Q|^2|\Psi_0^{(L)}\rangle. \qquad (12)$$

Note that the computation of these expressions only requires a knowledge of the lowest-state wave function of the angular momentum L subspace.

This method is usually employed in the study of nuclear giant resonances[32,33] and was used in Ref. 19 to obtain upper bounds to the first $L=0$ excitation, as well as to the low-lying even-L states. Since the $L\neq 0$ excitations can be obtained directly from the DMC procedure, the sum rules method will be used here to estimate the energies of the first $(n=1)$ excited vibrational states in each L subspace.

The upper bound given by Eq. (9) is a functional of the operator Q, so it may be variationally optimized by equating to zero its functional derivative with respect to Q. Unrestricted minimization will give rise to the unpractical relation $Q|\Psi_0^{(L)}\rangle=|\Psi_1^{(L)}\rangle$, its solution being equivalent to the solution of the many-body Schrödinger equation for the excited state. An alternative is to optimize the operator inside a restricted subspace, following the Feynman and Cohen[34] treatment of compressional excitations in liquid ^{4}He. This is the approach followed by Chin and Krotscheck[8,35] and also by Krishna and Whaley.[18] When $\Psi_0^{(L)}$ is the exact wave function of the lowest L state, a rigorous upper bound is obtained for the energy of the first excited state.

To calculate the monopolar excitations of each L state, including the ground state with $L=0$, the corresponding operator has been expanded as

$$Q(\mathcal{R}) = \sum_{p=1}^{5} c_p \sum_{i<j} r_{ij}^p,$$

where $r_{ij}=|\mathbf{r}_i-\mathbf{r}_j|$ is the distance between the (i,j) pair of atoms. The parameters c_p have been optimized so as to obtain the lowest upper bound to the first excited state for each angular momentum subspace. Note that the excitations obtained are approximate because mixed matrix elements are used to calculate the required moments, so the strict variational character is lost.

C. Importance-sampling wave functions

The following importance-sampling variational wave function for a system of N atoms was used:

$$\Phi_{\text{var}} = \prod_{i<j}^{N} e^{-g(r_{ij})}, \qquad (13)$$

which includes only two-body Jastrow correlations. Note that the wave function is translationally invariant. The correlation term was parametrized as

$$g(r) = p_1 r + p_2 \ln r + p_3 \frac{1}{r^2} + p_4 \frac{1}{r^{p_5}}. \qquad (14)$$

The last term recalls the familiar McMillan correlation factor,[36] which screens conveniently the strong short-range atom-atom repulsion. For the conventional Lennard-Jones potential the value $p_5=5$ should be used. For the Aziz interaction used in the present investigation the parameters p_4 and p_5 were fixed, independent of the number of atoms, to the values

$$p_4 = 138.6898 \text{ Å}^{p_5}, \quad \text{with } p_5 = 5.2,$$

according to our previous studies.[37] The remaining parameters p_1, p_2, and p_3 were optimally determined by minimizing the ground-state expectation value of the Hamiltonian for each cluster. In the interval between $N=3$ and 50, these parameters can be well fitted by the following second-order polynomials:

$$p_1 = -6.31 \times 10^{-2} + (2.55 \times 10^{-4}N) - (3.92 \times 10^{-5}N^2),$$

$$p_2 = -0.621 + (2.81 \times 10^{-2}N) - (2.90 \times 10^{-4}N^2),$$

$$p_3 = -1.93 + (4.18 \times 10^{-2}N) - (2.71 \times 10^{-4}N^2),$$

if r in Eq. (14) is given in Å. The energies were computed by the standard variational Monte Carlo (VMC) procedure, with a random walk of Metropolis type.[38] The Metropolis step was adjusted so as to have an acceptance ratio between 0.6 and 0.7.

The comparison of VMC energies with the statistically exact DMC ones, shows that the agreement deteriorates with increasing N, revealing the importance of three-body correlations when the density of the system grows. Three-body correlations, however, are not included in our variational wave function, with the objective of having a fast DMC algorithm. In any case, their effect will be incorporated along the stochastic random walk.

D. Computational details

In the DMC calculations the step time was taken to be $\tau=10^{-4}$ K^{-1}, after checking that it was sufficiently small to neglect the discretization correction. To stabilize the system, 2.5×10^4 τ steps were required, which corresponds to an elapsed time of $T_{stab}=2.5$ K^{-1}, for which the admixture of a state at an excitation energy of, say, 3 K, typical of the first monopolar excitation, will be diminished by a factor 5 $\times10^{-4}$. The energy expectation value versus the number of steps decreases exponentially at the beginning and already after some 10^3 steps is stable within the statistical fluctuations. Afterwards, the DMC evolution was pursued along 5 $\times10^4$ more steps, during which the relevant physical quantities were sampled.

The initial number of walkers was 10^3. This number may increase or decrease along the DMC steps, so that it was stabilized every 50 steps. The value of the energy E controlling the replication of walkers was adjusted also every 50 steps with the current sampling average. Final results thus correspond to about 5×10^6 samples. Averages obtained after a single time step were grouped with an increasing number of time steps, until the variance remained constant. Empirically it was found that grouping in blocks of 500 steps was adequate to minimize the effect of correlations in the DMC process.

Some of the above parameters may seem unnecessarily large, which certainly is the case for the light clusters, with less than about ten atoms. However, a very high precision was required since for comparison with the experiments the exact size of the cluster at which the excitation energy crossed the chemical potential curve had to be accurately determined. Since both curves are nearly horizontal, small errors in the energies lead to large shifts in the value of N at crossing. As mentioned earlier, the importance-sampling Jastrow function, with only two-body correlations, is quite good for the light systems, but is not so accurate for N larger than 20. This simple form was maintained because every DMC step required $O(N^2)$ operations, and using more accurate importance-sampling wave function with three-body correlations would have required $O(N^3)$ operations, making the calculations too long for the present step-by-step analysis. Thus it was necessary to compensate for these deficiencies by brute force sampling. Also, the adopted time step τ is very small for light systems. It should be mentioned that moving, say, ten particles in a Gaussian of width $\sigma=2\sqrt{D\tau}$ ≈0.05 Å corresponds to a very small change in the wave function for a small system, but is a relatively large step for a cluster with 40 or 50 particles.

III. THE ENERGY LEVELS OF ^{4}He CLUSTERS

A. Ground-state energies

The calculated ground-state energies $E_0^{(0)}$ are plotted in Fig. 1 for $N=3-50$. The curve shows a smooth shape without any evidence for "magic" stabilities related to a local increase of the binding energy.

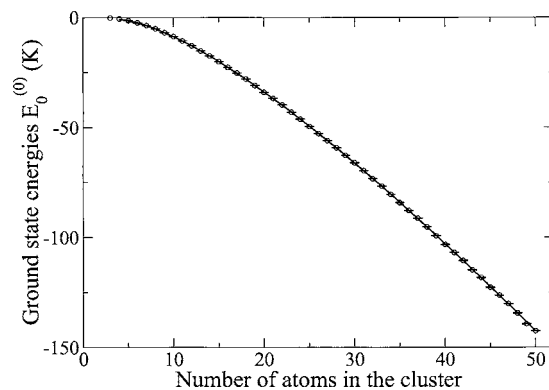To calculate the chemical potential it is convenient to

FIG. 1. The ground-state energies $E_0^{(L=0)}$ as a function of N. The circles are the direct result of the DMC simulations, and the continuous line is a fit of these results with the liquid-drop formula Eq. (15).

eliminate the statistical fluctuations by fitting the DMC-calculated ground-state energies to a three-parameter liquid-drop formula,

$$E_0^{(0)}(N) = A_v N + A_s N^{2/3} + A_c N^{1/3}, \qquad (15)$$

with the familiar volume (A_v), surface (A_s), and curvature (A_c) terms. The adjusted parameters are given in Table I. The obtained χ^2 per datum is close to 1 which corresponds to an acceptable fit. It is interesting to note that the volume term ($A_v=-7.84$ K) is rather close to the experimental value -7.17 K (Ref. 39) of the bulk binding energy per particle. However, it is sufficiently different to conclude that droplets of up to 50 atoms are still far from the behavior expected for a large liquid drop. The quality of this fit is shown in Fig. 1, where it is compared with the DMC-calculated energies.

The first relevant quantity for our study of the excited states is the energy needed to evaporate one atom, usually denoted as the chemical potential

$$\mu(N) = E_0^{(0)}(N) - E_0^{(0)}(N-1). \qquad (16)$$

Because μ defines the energetic region in which excited states are stable, its dependence on the number of particles N was analyzed. The calculated chemical potentials are plotted in Fig. 2 as a function of the number of atoms N in the cluster. The fluctuations seen in Fig. 2, especially for the larger clusters, result from the inherent statistical errors of the direct DMC calculations of the ground-state energies. Thus the small practically invisible error bars in Fig. 1 be-

TABLE I. Liquid-drop formula fit [Eq. (15)] parameters (in K) of the lowest energies of states with angular momentum L. The fit range and the obtained χ^2 are also quoted. The row labeled ΔE_0^* is the fit to the monopolar excitation energy of the ground state.

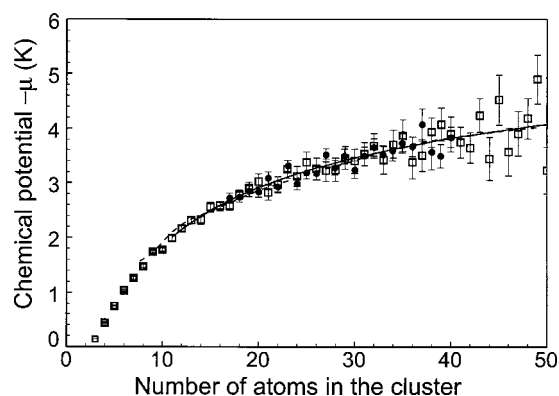| L	Range	χ^2	A_v	A_s	A_c
0	10 - 50	47	−7.842	23.126	−17.423
1	30 - 50	43	−7.483	20.497	−11.559
2	10 - 50	82	−7.825	22.768	−16.047
3	10 - 50	105	−7.923	23.247	−16.265
4	20 - 50	48	−7.826	22.568	−14.837
5	39 - 50	39	−8.625	28.017	−23.876
ΔE_0^*	10 - 50	50	−0.198	1.149	−0.571

FIG. 2. The chemical potential μ as a function of N. The squares are obtained from the direct result of the DMC simulations, and the continuous line is a fit of these results. The filled circles are the simulations of Ref. 40 and the dashed lines (almost coincident with the continuous line) are the density-functional results of Ref. 41.

FIG. 3. The excitation energies of the calculated (n,L) levels as a function of N for $N \lesssim 50$. The energies increase in going from left to right and from top to bottom. The squares with error bars are the direct differences of the DMC simulations. The dashed line represents the chemical potential limit.

come quite large in Fig. 2 when the differences required by Eq. (16) are calculated. In order to improve the quality of the determination of μ it would have been necessary to either substantially increase the number of samples, and correspondingly the computation time, or start from more precise importance-sampling wave functions, for example, by including triplet Jastrow correlations. Instead, because of the already large computing time, the smoothed energies were fitted with Eq. (15) and the differences $E_0^{(0)}(N) - E_0^{(0)}(N-1)$ were calculated. The smoothed results are also plotted in Fig. 2 as a solid line.

For comparison with the present calculations the results (filled circles) of the DMC calculation of Sola *et al.*[40] using the same Aziz interaction as well as the chemical potential (dashed line) calculated within the Orsay-Trento (OT) finite-range density functional of Dalfovo *et al.*[41] are also plotted in Fig. 2. Notice that the dashed line can barely be distinguished from the solid line fit of our DMC results. All the calculations confirm earlier results[13,40,41] that there are no significant abrupt discontinuities in the chemical potential of ^{4}He clusters, and magic numbers associated with small changes in stabilities are not expected.

B. Lowest excited states

The same smoothing procedure has been used to analyze the energies $E_0^{(L)}$ and $E_1^{(L)}$ in each L subspace. These energies were also fitted with the functional form of Eq. (15), and afterwards the corresponding excitation energies

$$\Delta E_L(N) = E_0^{(L)}(N) - E_0^{(0)}(N)$$

and

$$\Delta E_L^*(N) = E_1^{(L)}(N) - E_0^{(0)}(N),$$

were obtained from the difference between the respective fitted curves. Although in this case the resulting fit parameters no longer have any obvious physical meaning, their values are also included for completeness in Table I. The upper bounds obtained for the $(1, L)$ levels are, with the exception of the $L=0$ state, always above the chemical potential limit and therefore correspond to unstable clusters.
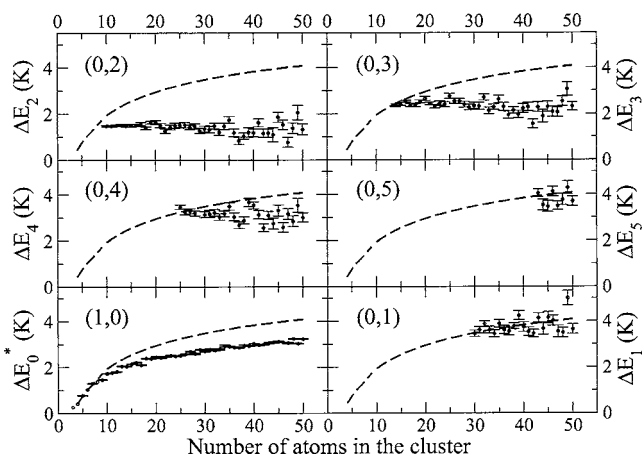
For this reason the corresponding results are not quoted in this paper.

The excitation energies of the lowest states $(0, L)$ with angular momentum $L=1$–5 as well as the first vibrational excitation level $(1, 0)$ are plotted in Fig. 3 as a function of the number of atoms in the cluster. For comparison the absolute value of the chemical potential has also been plotted as a dashed line. It is interesting to note, that in Fig. 3 some of the excitation levels lie above the chemical potential limit for some values of N. If our DMC calculations were really free of constraints, states with N atoms above the evaporation limit should result in a simple pattern: a bound subsystem of $N-1$ atoms and a single particle far away from the $N-1$ cluster, with a relative motion which conserves the total angular momentum of the N atom cluster. However, the importance-sampling methodology, needed to control the variance and more importantly to assure a positive definite quantity which can be interpreted as a probability distribution function, strongly constrains the DMC randomization process. Since the variational projection wave function is localized, the DMC combination of drift, isotropic diffusion, and rate terms will not be able to describe the removal of a single particle very far away from the remaining $N-1$ cluster, unless the total elapsed time becomes unreasonably large. Nevertheless, it is interesting to note that those unbound excited states, physically irrelevant, attain an energy quite close to the evaporation limit and thus to the threshold of the unbound system.

It can be seen in Fig. 3 that the lowest excitation corresponds to the $(0, 2)$ level and that it is stable for $N \simeq 8$ and onwards. The next excited level with $(0, 3)$ starts to be bound at $N \simeq 14$ and the following level with $(0, 4)$ appears at $N \simeq 25$. The remaining levels require a more extended discussion.

The $(0, 5)$ level appears to be bound for $N \approx 41$ and onwards. Unfortunately this is the region where the error bars are very large, and it is not possible to define more precisely the crossing point. For the $(1, 0)$ level the present calculations simply predict an approximate upper bound to the excitation energy due to the use of mixed matrix ele-

TABLE II. Monopolar (L=0) and quadrupolar (L=2) excitation energies and chemical potential (μ) obtained from various methods for clusters with N=20 and N=40 atoms. The row labeled DFT is a RPA calculation of Ref. 42. The rows DMC-I and DMC-II are two DMC calculations of Ref. 8 using the Aziz HFDHE-2 interaction. All energies are in K.

	N=20			N=40		
	L=0	L=2	−μ	L=0	L=2	−μ
DFT	2.6	1.6	2.86	3.2	1.3	3.81
DMC-I	2.72	1.75	2.91	3.60	1.37	3.67
DMC-II	2.80	1.71	2.91	3.68	1.22	3.67
This work	2.38	1.48	2.92	2.99	1.30	3.82

ments. The crossing of this level is not very well defined, it lies somewhere in the interval N=6–8. With increasing N the monopolar excitation energies lie just below the chemical potential curve. Finally, the (0, 1) excitation is special. As commented above, this is an abnormal excitation mode, mainly due to the center-of-mass constraint which forces the use of a rather unnatural importance-sampling wave function. The directly calculated results, Fig. 3, as well as the liquid-drop fit (Table I) are so close to the dissociation limit that one cannot conclude from the present calculations that this level is bound.

Our results are compared with several other calculations, which are only available for a few values of N, in Table II. The random-phase approximation (RPA) calculations of Ref. 42 based on the OT finite-range density functional,[41] which appear in Table II in the row labeled DFT, were taken from Figs. 5 and 8 of Ref. 42. They agree better for N=40 than for N=20 as might be expected for a density-functional theory (DFT) calculation. It should be kept in mind that the density-functional results suffer from the center-of-mass motion problem which is only approximately corrected in the ground-state properties. It is nevertheless interesting to see that the density-functional method gives results reasonably close to the DMC ones.

The DMC calculations of Chin and Krotscheck[8] are also in satisfactory agreement with the present calculations, although one should keep in mind that the atom-atom interac-

tion is not the same, as these authors employed the older Aziz HFDHE-2 interaction.[43] Chin and Krotschek performed two different calculations, based on two different importance-sampling wave functions: DMC-I only contains Jastrow pair correlations while DMC-II also includes triplet correlations. They fitted their chemical potential to the binding energies calculated for N=20, 40, 70, and 112. This can explain the slight differences between their result and ours.

As seen in Table II the present excitation energies with the only exception of the N=40, L=2 level are significantly smaller than in Ref. 8 by about 16%–20%. These differences between the DMC results testify to the difficulties in obtaining precise values for quantities other than the ground-state energies. Also it is worth recalling that in Ref. 8 the Feynman eigenvalue problem was solved in order to calculate the excitation energies; in this process a discretization of the multipolar expansion of the the two-body density was required, which is a delicate numerical problem, not exempt of uncontrolled uncertainties.

In order to ascertain the sensitivity of these results to the He–He interaction, the clusters N=3–10 were also computed using the LM2M2 (Ref. 25) and TTY (Ref. 26) interactions. The results for the ground-state energies, chemical potentials, and monopolar excitation energies are displayed in Table III. Although the differences in the binding energies are only about 2%–3% different values by up to about 20% are found for the TTY chemical potential for N=5, 6, 7, and 8. The only cases where there is some sensitivity correspond to the ground-state energy of the trimer, and to the threshold of stability of the monopolar excitation, which is N=8, 6, and 7 for HFD-H(HE), TTY, and LM2M2, respectively.

The monopolar excitation of light ⁴He clusters has also been studied by Blume and Greene.[44] These authors employed the adiabatic hyperspherical approximation to formulate a Schrödinger-type equation in terms of the hyperradius collective variable $\sum_{i<j}(\mathbf{r}_i - \mathbf{r}_j)^2$, which allows for the determination of an upper bound to the ground-state energy, as well as an estimate of the monopolar excitation energy. The hypercentral potential entering the adiabatic equation was obtained by these authors after performing a DMC calcula-

TABLE III. Comparison between DMC calculations for ground-state binding energies (E_0), chemical potentials (μ), and monopolar excitation energies (ΔE_0^*) obtained with the indicated interactions. The last column includes the values obtained with the hyperspherical approximation. All energies are in K.

	HFD-H(He)[a]			TTY[b]			LM2M2[c]			
N	$-E_0$	$-\mu$	ΔE_0^*	$-E_0$	$-\mu$	ΔE_0^*	$-E_0$	$-\mu$	ΔE_0	ΔE_0^{*d}
3	0.135(2)		0.27	0.136(6)		0.14	0.124(2)		0.12	0.123
4	0.573(2)	0.442	0.42	0.561(3)	0.425(7)	0.58	0.558(3)	0.434(4)	0.55	0.427
5	1.334(2)	0.661	0.78	1.304(4)	0.743(5)	0.72	1.310(5)	0.752(6)	0.88	0.712
6	2.367(3)	1.033	1.04	2.317(6)	1.013(7)	0.93	2.308(5)	0.998(7)	1.07	0.982
7	3.646(4)	1.279	1.30	3.357(7)	1.040(9)	1.25	3.552(6)	1.244(8)	1.24	1.229
8	5.144(5)	1.498	1.38	5.057(11)	1.700(13)	1.34	5.030(8)	1.478(10)	1.45	1.391
9	6.827(6)	1.683	1.47	6.667(8)	1.610(14)	1.49	6.679(9)	1.649(10)	1.53	1.553
10	8.673(6)	1.846	1.73	8.548(12)	1.881(14)	1.81	8.532(10)	1.853(13)	1.66	1.807

[a]Reference 24.
[b]Reference 26.
[c]Reference 25.
[d]Reference 44.

tion using the LM2M2 interaction. Our DMC ground-state energies obtained with the LM2M2 interaction are essentially the same as those given by Blume and Greene, as should be expected. However, Blume and Greene found that the monopolar excitation $(1, 0)$ is stable for all clusters $N \geqslant 3$, in contrast to our threshold at $N \geqslant 7$. This is an important difference and raises a very interesting question both from the theoretical and the experimental viewpoints. Both calculations, the one based on the moment method and the other based on the hyperspherical description, are, however, approximate, because they rely on the use of *mixed* matrix elements.

IV. ANALYSIS OF ABUNDANCES IN FREE JET EXPANSIONS OF ^{4}He

As mentioned in the Introduction, the detailed calculations described above were in part motivated by the unexpected observation of a number of maxima in the measured distribution of ^{4}He cluster sizes up to about $N \simeq 70$. These clusters were produced in a free jet expansion of the cryogenically cooled gas through a $D=5 \ \mu$m diameter thin-walled orifice into vacuum.[47] The size distributions were measured by diffracting the beam of atoms and clusters from a nanostructured transmission grating.[45,46] According to the constructive interference condition the first-order diffraction peaks are given by

$$\theta_N \simeq \frac{\lambda_N}{d} = \frac{h}{Nmvd}, \tag{17}$$

where λ_N is the de Broglie wavelength of a cluster consisting of N atoms, m is the mass of a ^{4}He atom, v is the cluster velocity, and d is the period of the SiN$_x$ grating, which is 100 nm.[45] In the past this technique was limited to the resolution of clusters differing in size by one atom up to about $N \simeq 6$, although some evidence for weak magic numbers up to about 26 was found.[47] In the new experiments the angular resolution was increased from typically $\Delta\theta_N$ [full width at half maximum (FWHM)] $\simeq 80$ to $20 \ \mu$rad. To take full advantage of the improved resolution a low source temperature of $T_0 = 6.7$ K corresponding to a relatively large atom de Broglie wavelength of $\lambda_1 = 4.0$ Å was used in the new experiments. Figure 4 shows a series of diffraction patterns taken with the grating in the position of normal incidence and tilted with respect to the incident beam by two different angles of inclination.[45] As discussed elsewhere[45] under these conditions the resolution increases, but also because of the narrowing of the effective grating slit widths, the slit function is modified in such a way that higher-order peaks are enhanced. In addition the van der Waals interaction with the bars is reduced.[48] In these patterns maxima of intensity are clearly visible at 9 and 10, 14 and 15 and more broad peaks at 26 and 27 and 44±4. The large central maximum at $\theta=0$ is due to the ubiquitous specular peak. Similar magic numbers are seen in the five angular distributions for normal incidence measured for a series of source pressures presented in Fig. 5. The patterns at highest pressures in Fig. 5 reveal additional maxima at 65±5 and 73±6.
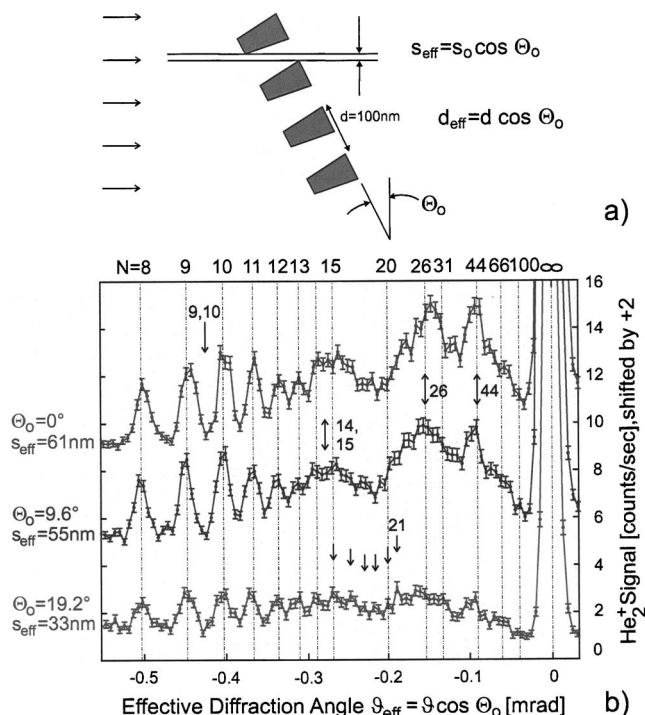

FIG. 4. Experimental helium cluster diffraction patterns (b) measured for normal incidence on the grating and two different angles of inclination θ_0 at $T_0 = 6.7$ Å and $P_0 = 1.25$ bar. The angle of inclination and the effective width s_{eff} and period d_{eff} are defined in (a). The angles in the bottom abscissa in (b) have been corrected so that clusters with same number of atoms N (top abscissa) lie at the same angle. The intensity scales in (b) are shifted by 4 counts/s. Magic numbers are identified at 9 and 10, 14 and 15, and about 26 and 44. Single peak are resolved up to $N=21$ in the $\theta_0=19.2$ measurement.

The pronounced shift in the overall maximum of these distributions with source pressure is somewhat reminiscent of that reported for He$_2$, He$_3$, and He$_4$ in Ref. 47, but at higher source pressures. Thus the shift of the relative intensities to smaller diffraction angles with increasing source pressures reflects the further progression of homogeneous nucleation to larger clusters. Despite this systematic shift in relative intensities the features persist throughout the range of source pressures are explored. This suggests that the features reflect an inherent enhancement related to the clusters themselves and are not falsified by other spurious effects.

The same structures were found in diffraction experiments carried out at $T_0 = 4.1$ K, but at a correspondingly lower source pressure of $P_0 = 0.385$ bar. Diffraction patterns were also measured for electron-impact energies between 70 and 400 eV and confirmed the same structures with only minor differences in the peak-to-valley intensity ratios. Thus all the magic numbers were found to be very robust and independent of these conditions.

More insight into the actual magnitudes of the magic number maxima is provided by transforming the angular distributions to the true population distributions in the beam. This requires a number of corrections of the relative diffraction intensities to account for (1) the size dependence of the overall ionization cross section, (2) the probability that the detected He$_2^+$ ions are formed upon ionization of a neutral cluster of a certain size, and (3) the effect of the van der Waals interaction with the grating bars.
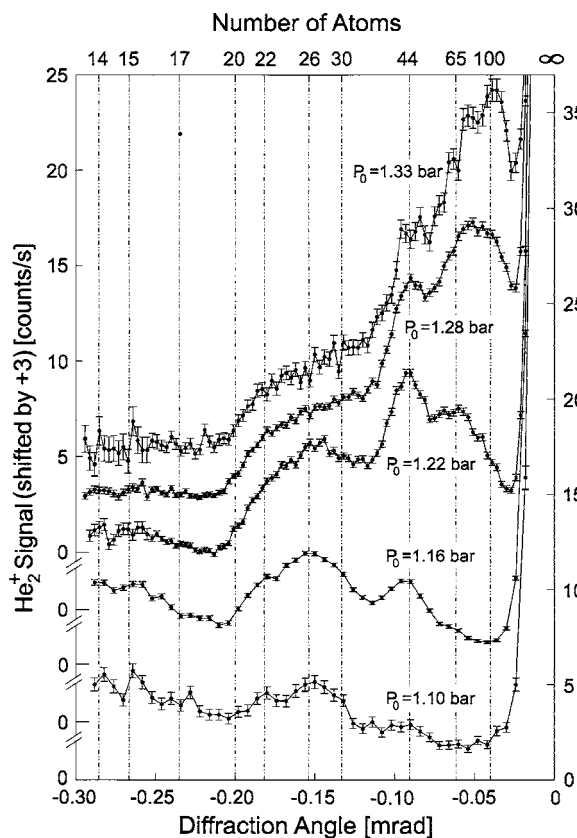
FIG. 5. Experimental helium cluster diffraction patterns measured for normal incidence at $T_0 = 6.7$ K and for five different source pressures P_0, for diffraction angles corresponding to $N = 14$ up to about 100 as indicated in the top abscissa. Magic numbers are seen at about $N = 26$, 44, and at 65–100 for $P_0 \geq 1.22$ bar.
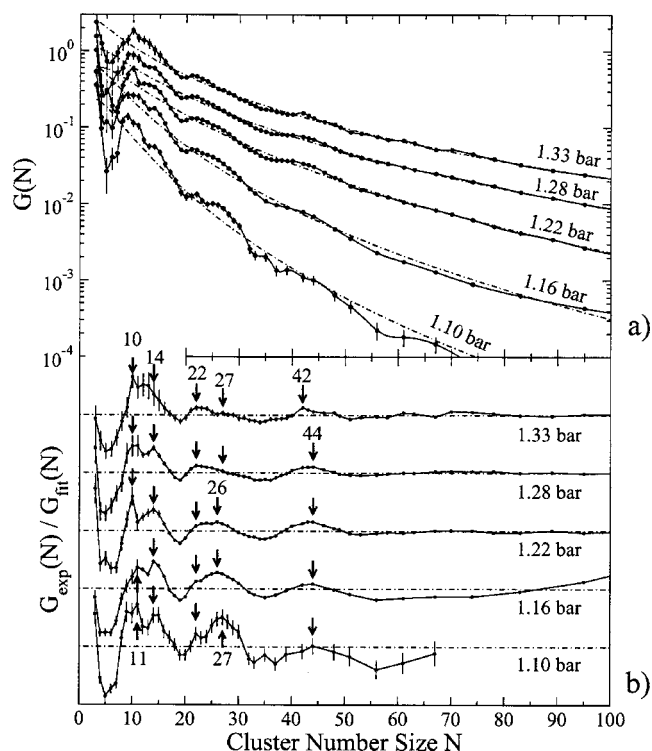

FIG. 6. (a) ^{4}He cluster size distributions $G(N)$ obtained from a transformation of the diffraction patterns in Fig. 5 as described in the text. The sharp dropoff in the average distributions at large sizes N is caused by the N^{-2} factor in the Jacobian of the transformation and N^{-1} correction of the ionization cross section. (b) The ratio of the $G(N)$ distributions to the asymptotic distributions $G_{\text{fit}}(N)$ [dotted-dashed curves in (a)]. Maxima in the cluster size distributions are clearly seen at $N = 10$ and 11, 14, 22, 26 and 27, and 44. The statistical errors are indicated by the vertical lines.

The ionization cross section is assumed to be equal to N times the ionization cross section of a single atom. This dependence has been confirmed by theory and experiment for He_2, N_2 and CO_2 clusters[49] and is not unexpected in view of the smallness of the ionization cross section ($\approx 10^{-16}$ Å^2) compared to the geometrical size of the clusters ($\approx 50 \times 10^{-16}$ Å^2). The probability that the corresponding He_2^+ fragmentation ion is formed upon ionization of a given neutral cluster, measured previously to be 5%, 40%, 70%, 70%, and 75% for $N = 2$–6, respectively.[47] For larger clusters with $N \approx 100$ there is evidence that 70% of the cluster-ion fragments are He_2^+.[50] Thus the He_2^+ distribution measured on mass 8, I_8, is not expected to be significantly distorted compared to the neutral cluster distributions and provides a signal proportional to the intensity of the neutral clusters for all N.

The effect of the van der Waals interaction of the clusters with the grating bars is estimated by assuming the C_3 interaction constant of the cluster to be $C_3(N) = NC_3(1)$, where $C_3(1)$ is the atom-surface interaction constant which has been measured with the diffraction method.[48] The theory of Ref. 48 is used to calculate the intensity of the first-order diffraction peaks and thus recover the incident intensity. The geometrical size of the cluster was only accounted for in the case of He_2 and He_3, which have average bond distances of 52 and 9.6 Å, respectively.[51] The larger He clusters are more compact and the effect of their sizes is smaller than the van der Waals correction.

As discussed in the earlier report[15] these corrections can be performed with sufficient precision and are not expected to significantly affect the relative intensities of the individual magic numbers with respect to adjacent cluster sizes.

Whereas for the resolved part of the diffraction pattern ($N \leq 11$) the individual peak intensities can be calculated by integrating over the individual peak profiles, for the unresolved region ($N > 11$) an additional correction was required. To account for the inverse dependence of N on the diffraction angle, the population distributions $G(N)$ were calculated from the corrected He_2^+ angular distributions $I_8^*(\theta)$ via the following formula:

$$G(N(\theta)) = I_8^*(\theta) \left| \frac{d\theta}{dN} \right| = I_8^*(\theta) \frac{\lambda_1}{d} N^{-2}, \tag{18}$$

where $(\lambda_1/d)N^{-2}$ is the Jacobian $|d\theta/dN|$ calculated from Eq. (17).

Figure 6 compares the $G(N)$ distributions derived from the experimental diffraction patterns presented in Fig. 5 with best-fit theoretical asymptotic distributions:[52]

$$G_{\text{fit}}(N) = ZN^a e^{-bN}, \tag{19}$$

The good average agreement with the $G_{\text{fit}}(N)$ distributions is especially gratifying since it has been predicted by theoretical models of cluster growth.[52] Figure 6(b) shows the ratios of the actual $G(N)$ distributions to the smooth $G_{\text{fit}}(N)$ distributions. These ratios provide a direct measure of the magic

TABLE IV. Comparison of experimental magic numbers determined from the angular distributions $I(\theta)$ and from the $G(N)$ distributions with the theoretical values Z_N/Z_{N-1}. The ±1 uncertainties in the last row result from the estimated standard deviations of the excitation energies.

$I(\theta)$	9 and 10	14 and 15	22	25–27	42–46
$G(N)$	10 and 11	14	22	26 and 27	44
Z_N/Z_{N-1}	8±1	14±1	⋯	25±1	44±1

number effect on the cluster size distributions and clearly reveal the magic numbers, which are summarized in Table IV. It is important to note that the broad maxima at $\dot{N}$ =65(P_0=1.22 bar) and N=75(P_0=1.28 bar) seen in Fig. 5 do not appear in Fig. 6 and, in fact, are not true magic numbers. These maxima can be explained by noting that in order to obtain angular distributions corresponding to $G(N)$ distributions, the latter have to be multiplied by a factor of N^3 to account for both the Jacobian entering Eq. (18) as well as the size dependence of the ionization cross sections. This explains the broad peaks at small angles in the angular distribution for P_0=1.22, 1.28, and 1.33 bar in Fig. 5.

Initially it was expected that these magic numbers might be explained by some small enhancement in the stabilities which might have gone undetected in earlier calculations. The new detailed highly accurate binding energies and the chemical potential presented in Figs. 1 and 2, however, definitely rule out this possibility. The new accurate N-resolved calculations of excited energy levels reveal, however, an interesting coincidence between the intersections of the excited level curves with the chemical potential and the experimentally observed magic numbers.

The link between the level crossings found in the calculations and in the experimental magic numbers is provided by considering the mechanism by which clusters are formed in the free jet expansion. Virtually all theories of the kinetics of homogeneous nucleation assume that cluster growth is dominated by the following three-body reaction:

$$\text{He}_{N-1} + \text{He} + X \leftrightharpoons \text{He}_N + X, \qquad (20)$$

where X is a spectator particle required to fulfill the energy and momentum conservation laws. As is well known the frequency of atom collisions to form clusters drops rapidly in the initial stages of the gas expansion[53] since the density decreases roughly as z^{-2}, where z is the distance from the orifice. Typically, after a reduced distance of only about $z/D \simeq 2$, where D is the orifice diameter, three-body collisions no longer occur, and two-body collisions cease after about $z/D \simeq 10$.[53] In the well-known sudden freeze model used to describe the rotational and vibrational temperatures of the molecules in gas expansions it is assumed that the underlying inelastic collision processes instead of falling off gradually are terminated at some fixed point in the downstream flow. Here it is assumed that the equilibrium processes associated with cluster growth are also abruptly terminated. The frozen equilibrium is then assumed to be maintained by further downstream since the remaining two-body collisions are too few in number or too feeble to affect the cluster size distribution. Finally it is important to note that model calculations of cluster growth have revealed a

direct correlation between anomalies in the equilibrium constants for the growth of clusters of a specific size and the abundances of clusters of the same size.[52] Confirmation of this model comes from recent diffraction measurements of the mole fractions of small mixed $^4\text{He}_m{}^3\text{He}_n$ clusters. By assuming effective equilibrium temperatures which increased smoothly with size N up to $N=m+n=7$ a close correlation with the predicted binding energies could be established.[54]

In the present context the expanding gas was described as an ideal-gas mixture of atoms and clusters of various sizes. The equilibrium constant related to Eq. (20) can then be given in terms of the partition functions,

$$K \equiv \frac{\Xi_N \Xi_X}{\Xi_{N-1} \Xi_1 \Xi_X} = \frac{\Xi_N}{\Xi_{N-1} \Xi_1}, \qquad (21)$$

which is independent of the spectator particle X. The partition function for each cluster is the product of the center-of-mass translational (Z_N) and internal (ξ_N) partition functions

$$\Xi_N = Z_N \xi_N. \qquad (22)$$

The center-of-mass translational partition function can be written as

$$Z_N = \frac{1}{h^3} \int d\mathbf{p}\, e^{-p^2/(2NmkT)} = (\lambda_T(N))^{-3}, \qquad (23)$$

where λ_T is the thermal de Broglie wavelength of a cluster:

$$\lambda_T(N) = \left(\frac{2\pi\hbar^2}{NmkT} \right)^{1/2}. \qquad (24)$$

The internal partition function is simply the sum of Boltzmann factors for the discrete bound levels of the cluster with N atoms

$$\xi_N = \sum_{j=0}^{n_{\text{bound}}} g_j e^{-E_j(N)/kT}, \qquad (25)$$

where g_j is the degeneracy of the jth level, and $E_j(N)$ is the energy of the bound level, which is a negative quantity. In our case, for a level of angular momentum L, the degeneracy is $g=2L+1$. To explain the magic numbers it is convenient to first extract explicitly the term associated with the ground state by substituting $E_j(N)=E_0^{(0)}(N)+\Delta E_j(N)$,

$$\xi_N = e^{-E_0^{(0)}(N)/kT} \left(1 + \sum_{j=1}^{n_{\text{bound}}} g_j e^{-\Delta E_j(N)/kT} \right), \qquad (26)$$

where $\Delta E_j(N)$ is the positive excitation energy of level j taken with respect to the ground-state energy $E_0^{(0)}$.

Since the equilibrium constant Eq. (21) is dominated by the quotient Ξ_N/Ξ_{N-1}, this ratio is examined in more detail,
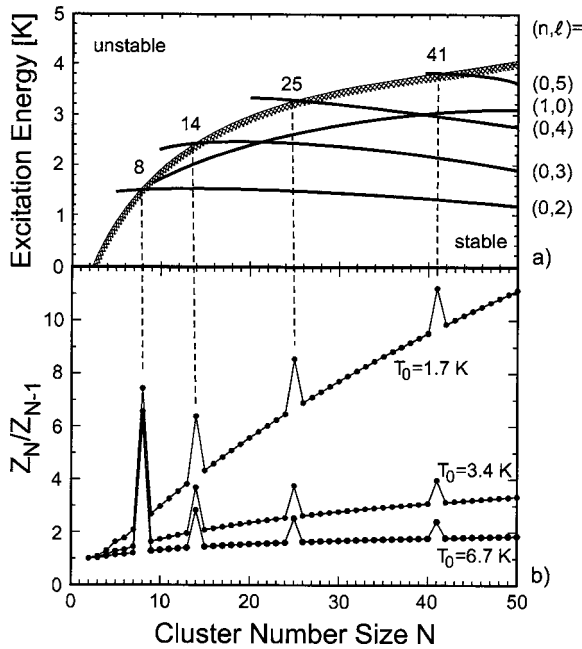
FIG. 7. (a) The energies E_j of the collective excitations for different values of the angular momentum and the chemical potential are plotted as a function of N. (b) The ratio of the partition functions Z_N/Z_{N-1} is plotted versus N. At the threshold values in (a) the ratio shows maxima.

$$\frac{\Xi_N}{\Xi_{N-1}} = \left(\frac{N}{N-1}\right)^{3/2} e^{\mu(N)/kT} \times \frac{1 + \sum_{j=1}^{n_{\text{bound}}} g_j e^{-\Delta E_j(N)/kT}}{1 + \sum_{j=1}^{n_{\text{bound}}} g_j e^{-\Delta E_j(N-1)/kT}}. \tag{27}$$

For cluster sizes with a certain fixed number of bound states $\mu(N)$ and $\Delta E(N)$ are smooth functions of N, and the quotient in Eq. (27) will also be a smooth function. However when for a size N^* an additional level becomes bound, then an additional term enters into the sum in the numerator on the right-hand side of Eq. (27) not present in the denominator. Thus the ratio is expected to jump sharply at $N=N^*$. For the next larger cluster N^*+1 both this cluster and the cluster with N^* atoms will have the same number of bound states once more and the quotient will be nearly the same as for $N < N^*$.

Before computing the partition functions the raw data on the energy levels shown in Fig. 3 were smoothed by fitting to the liquid-drop formula Eq. (15). The smoothed results are displayed in Fig. 7(a) together with the calculated chemical potentials. The N values at which the energy levels cross the chemical potential curve are also indicated in the figure. The (0,1) level has not been included since this level is assumed not to be bound, as explained in Sec. II B. The effect of the (1,0) level is minimal, since its threshold is almost superimposed on the (0,2) threshold. The exact position of the first three crossings is expected to have errors of about $\Delta N = \pm 1$. The value $N=41$, related to the (0,5) level, is the least precisely determined because of the large computational errors in the region of large clusters.

The partition function quotients Eq. (27) are plotted in Fig. 7(b) for three different assumed temperatures: T_0, the source temperature, and two lower temperatures close to the
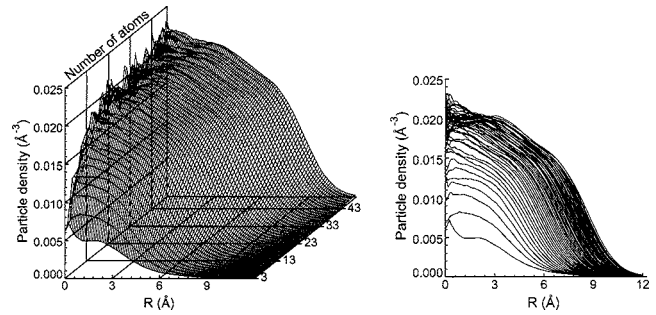

FIG. 8. The boson to center-of-mass distribution function $\rho(R)$ from $N=3$ to 50 in steps of 1, obtained from the direct DMC simulation.

actual values at which the cluster size distributions are expected to be frozen in. It is gratifying to find that the spikes occur at the same number sizes $N^* = 8$, 14, 25, and 41 for all three temperatures. Moreover as expected they agree with the sizes at which the excitation levels cross the chemical potential curve. Table IV compares the N^* corresponding to the spikes with the magic numbers based on the raw $I(\theta)$ data [Fig. 7(a)] and those from the $G(N)$ distributions. Remarkably satisfactory agreement is found for all the observed magic numbers with the exception of $N^* = 22$.

Thus contrary to our initial expectations these magic numbers are not at all related to enhanced ground-state binding energies at specific values of N. They are, in fact, stability thresholds related to the cluster sizes at which excited levels cross the chemical potential curve from above and become stabilized. Thus the good agreement of the experimental magic numbers with the crossing of the energy levels with the chemical potential confirms the precision of these calculated curves. As far as we are aware this is also the first experimental evidence for such a mechanism for the production of magic numbers. The reasonable agreement between the trend of the measured peak intensities with cluster size and the predicted spikes in Fig. 7 gives new support to the simple equilibrium model. The results also nicely confirm the predicted smoothed size distributions of larger clusters formed in free jet expansions.[55]

V. THE SHAPE OF THE DROPLETS

Additional insight into the structure of the droplets comes from one-body radial distribution functions $\rho(R)$, which are plotted in Fig. 8 as a function of the distance R from the center-of-mass of the droplet from $N=3$ to $N=50$. They correspond to particle densities since they are normalized to the total number of particles

$$\int d\mathbf{R} \rho(R) = N.$$

The erratic behavior seen near the origin is related to the large statistical errors resulting from the small volume in which the DMC points are sampled. The steady increase in the density at the origin from $N=3$ up to $N \geqslant 20$, where it is nearly constant and close to the value 0.0216 Å^{-3} of the bulk density is, however, reliable and has been reported previously.[7,8]
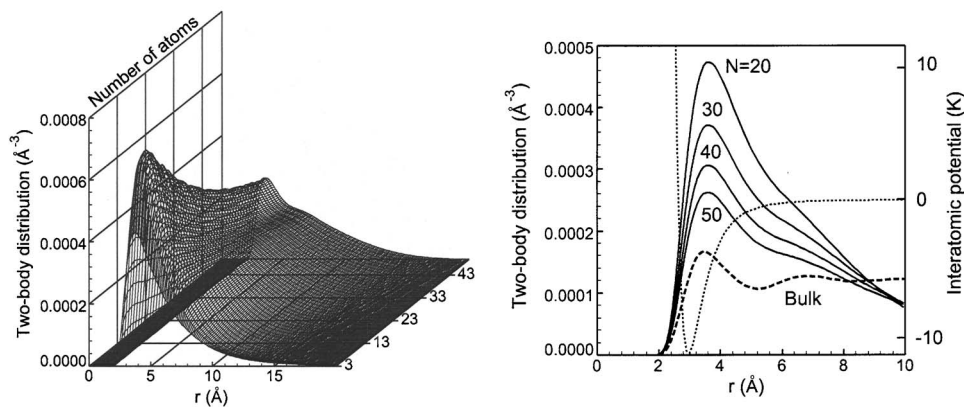
FIG. 9. Left panel: the boson-boson distribution function from $N=3$ to 50 in steps of 1, obtained from the direct simulation. The larger the number N, the longer the tail of the distribution, with a monotonic behavior. Right panel: the two-boson distribution function for $N=20$, 30, 40, and 50 atoms (solid lines). The experimental two-body correlation function is plotted (dashed line) on an arbitrary scale. The shape of the HFD-B(HE) two-body interaction employed in the calculation is also plotted (dotted line, left scale).

Many of the radial distributions exhibit slight oscillations in the falloff region. For $N \geq 10$ a first shoulder appears near the surface, and a second shoulder is also visible in the inner region for $N \geq 30$. These persistent oscillations have been previously observed for $N=70$ within a Green's-function Monte Carlo (GFMC) calculation[7] and for $N=70$ and 112 within a DMC calculation.[8] It was suggested that such oscillations could be a surface effect similar to the Friedel oscillations of electrons near the surface of a metal.[56] In their pioneering GFMC calculations,[7] Pandharipande *et al.* assumed these structures to result from spurious correlations along the stochastic random walk, but this has been ruled out by subsequent studies as well as by the present systematic analysis. Such oscillations might also reflect an underlying quasisolid structure which, although not included in the importance-sampling driving function, could be magnified by the DMC evolution. Similar oscillations are obtained employing the finite-range OT functional,[41] which incorporates a phenomenological short-distance repulsion. As the authors of Ref. 41 pointed out, these surface oscillations are related to the fact that the OT functional nicely reproduces the strong peak observed in the bulk static response function at the roton wavelength. However, the true origin of these density oscillations is still not understood.

Another quantity of interest is the two-body distribution function ρ_{BB}, which is the probability of finding a second boson particle as a function of the interparticle distance with respect to a given boson particle normalized in the following way:

$$\int d\mathbf{r} \rho_{BB}(r) = 1 .$$

Figure 9 shows a plot of the two-body distribution functions as a function of N (left panel). For some selected clusters they are also plotted in the left panel of Fig. 9 together with the two-body correlation function measured in the bulk.[57] The bulk correlation function is plotted on an arbitrary scale because of the different units and normalization of our two-body distribution functions. As a reference, the shape of the HFD-B(HE) interaction is also plotted. Notice that the short-range repulsion in the potential leads to a vanishing two-body density for a relative distance $r \lesssim 2$ Å, independent of N. The location of the first peak has a slight but noticeable shift, going from 3.75 Å for $N=3$ down to 3.6 Å for $N=50$. With further increase in size its position is expected to coin-

cide with that in the bulk. Beyond $N=30$ an additional shoulder is apparent at a relative distance of around 6–7 Å close to the second peak in the bulk. Finally, it is interesting to note that the two-particle density function at its maximum increases with size up to about $N \approx 20$, where it is nearly three times greater than in the bulk, before dropping off at larger distances. This effect is probably related to the centrosymmetric structure which leads to an initial compression of the small very weakly bound clusters. Beyond $N>20$ this compression is reduced since the particles can spread out over a greater volume.

The root-mean-square distances are displayed in Fig. 10. The upper curve corresponds to the relative distance between atoms, and the lower one to the distance between atoms and the center of mass. Also plotted are $N^{1/3}$-dependent fits for $N \geq 20$. Both distances decrease with decreasing N down to a minimum at $N=6$, and then increase sharply while approaching the mean distance of the dimer, which has been measured to be 52 ± 4 Å.[58] Thus the many-body additivity of the two-body potentials has a dramatic effect on reducing the interatomic distances.

VI. A MODIFIED LIQUID-DROP MODEL OF ELEMENTARY EXCITATIONS

The analysis of the normal modes of an incompressible liquid drop goes back to the 1879 work of Rayleigh.[59] His classical model can also explain the main features of the excitations of quantum systems such as the collective modes
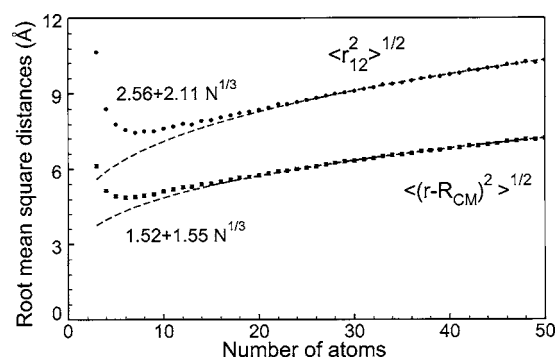

FIG. 10. Root-mean-square distances between atoms (circles, upper curve) and the center-of-mass (squares, lower curve) are plotted as a function of the number of atoms in the cluster. The dashed lines correspond to a $N^{1/3}$ fit of these distances for $N \geq 30$.

of atomic nuclei[60] and the elementary excitations of quantum fluid clusters.[61,62] The liquid-drop model gives reliable predictions for finite systems when the number of their constituents is sufficiently large. For small systems with some modifications the model is able to provide a simple physical model with which to explain the present microscopic DMC results.

In its simplest and usual form the liquid-drop model considers a sharp-edged spherical droplet of homogeneous fluid, characterized by the bulk particle density ρ_0 and a sharp step function radius $R_{\text{LDM}}=2.22N^{1/3}$ Å. The so-called equivalent uniform radius R_0 is related to the mean-square radius defined as

$$\langle R^2 \rangle = \frac{\int_0^\infty R^2 \rho(R) R^2 \mathrm{d}R}{\int_0^\infty \rho(R) R^2 \mathrm{d}R}, \tag{28}$$

and is given by the following relationship:

$$R_0^2 = \tfrac{5}{3}\langle R^2 \rangle, \tag{29}$$

which can be obtained by substituting $\rho(R)=\rho_0\Theta(R_0-R)$ into Eq. (28), where $\Theta(r)$ is the Heaviside step function. This radius is larger than R_{LDM} since it takes into account the actual density distribution of a finite-sized cluster which is smaller than ρ_0. With these boundary conditions the solution of the hydrodynamical equations gives rise to compressional and surface modes, whose excitation energies depend on N as $N^{-1/3}$ and $N^{-1/2}$, respectively.[61]

A. Surface modes

The $(n=0, L>0)$ excitations correspond to surface modes, described by ripplonlike oscillations with radial frequencies given by[59,61]

$$\omega = \left[\frac{\sigma_0}{m\rho_0 R_0^3} L(L-1)(L+2) \right]^{1/2}, \tag{30}$$

where $\sigma_0=0.354$ ergs/cm^2 is the surface tension[63] of the flat surface. Obviously this expression, which predicts a sharp rise in the frequencies with reduction in cluster radius and size, is in direct contradiction with the energy levels found here.

Tamura[64] is probably the first to consider the corrections needed to apply the liquid-drop model to small clusters. To account for the diffuse profile of the density, he assumed that the radial dependence of the particle density profile is described by a Fermi function
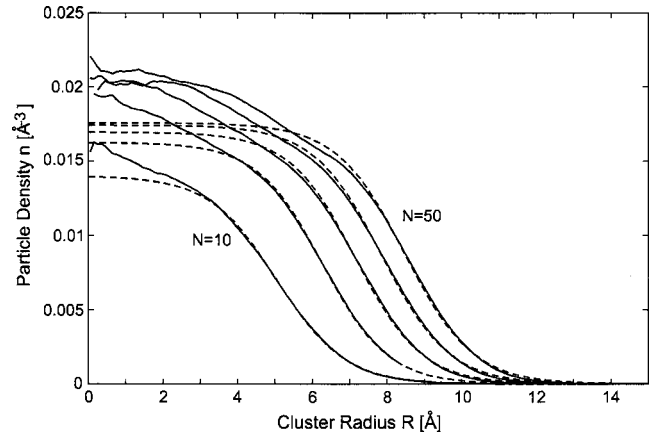

FIG. 11. DMC-calculated radial number density distributions for $N=10$, 20, 30, 40, and 50 plotted vs the distance to the cluster's center of mass. The dashed lines show best fits of the falloff region with the Fermi function Eq. (31).

$$\rho(R) = \frac{\rho_d}{1 + \exp\{(R - R_d)/d\}}, \tag{31}$$

where d is the falloff range of the surface density, which defines the width parameter $\tau = d/R_d$. Tamura thus derived the following modified Rayleigh formula:

$$\omega = \left[\frac{\sigma_{\text{dyn}}}{m\rho_d R_d^3} \frac{L[(L-1)(L+2) + (4\pi^2/3)\tau^2]}{1 + (\pi^2/3)\tau^2 L(2L+1)} \right]^{1/2}, \tag{32}$$

where σ_{dyn} is a *dynamical* surface tension which will be discussed below. This expression is valid within second order in τ. For large droplets, τ goes to zero, and this equation reduces to Eq. (30).

Figure 11 compares some of the DMC-calculated radial density distributions (Fig. 8) for sizes from $N=10$ to 50 in steps of 10 with best fits using Eq. (31).[27] The Fermi function in Fig. 11 provides an excellent fit of the important surface region, but breaks down in the central region. Since Tamura's derivation of Eq. (32) is most sensitive to the region around R_d the inner deviations are not expected to affect the results. The 90%–10% falloff width is about 4 Å, which is somewhat smaller than the width of 6.4 ± 1.3 Å measured for larger droplets consisting of 10^3–10^4 atoms.[65] For these small clusters, however, the width becomes comparable to the cluster radius and can be expected to have a big effect on the surface excitations. The best-fit parameters are summarized in Table V where the radius R_d is compared with the liquid-drop model radius R_{LDM} and R_0 as defined in Eq. (29).

A comparison of Eq. (32) with the present DMC excitation energies provides much better results than Eq. (30), but

TABLE V. Best-fit parameters of DMC radial density distributions and other measures of ^{4}He cluster radii.

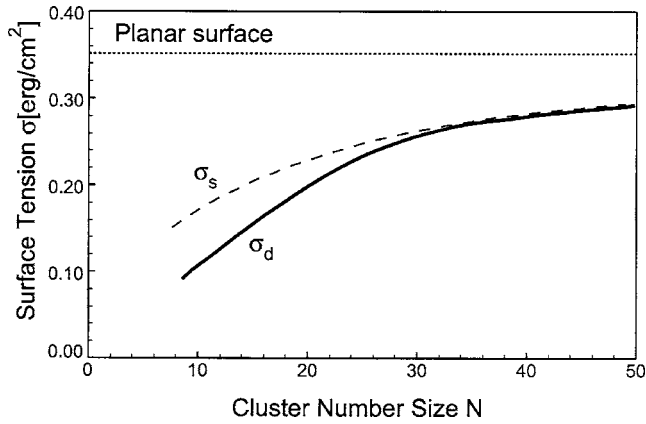| N	ρ_d (Å^{-3})	d (Å)	R_d (Å)	R_{LDM} (Å)	R_0 (Å)
10	0.0140	0.909	5.06	4.78	6.61
20	0.0163	0.877	6.27	6.03	7.44
30	0.0169	0.887	7.16	6.90	8.17
40	0.0174	0.906	7.85	7.59	8.82
50	0.0174	0.912	8.48	8.18	9.36

FIG. 12. Comparison of surface tensions. The static surface tension (dashed line) is compared with the best fit of the energy levels using Tamura's expression (solid line).

still diverges for small N. Apparently Tamura's equation should be corrected for other finite-size effects. One possibility for improving the fit is to treat σ_{dyn} as an adjustable parameter, which can be fitted to reproduce, for each N, the set of calculated DMC excitation energies. It is indeed quite remarkable to see that this leads to a uniquely defined smooth curve for σ_{dyn} as a function of N (Fig. 12) and that this curve is able to reproduce nicely the excitation curves for each of the $(n,L) = (0,2)$, $(0,3)$, and $(0,4)$ levels over their entire ranges of N. The agreement with the $(0,5)$ level is not so good, but is also satisfactory in view of the uncertainties in the calculated curves. The resulting best-fit curve in Fig. 12 decreases with decreasing N and extrapolates to $\sigma=0$ as $N \rightarrow 0$ as expected. Since this surface tension is determined from the elastic stretching response it has been designated here as a dynamic surface tension σ_{dyn}.

The present calculations here also provide the possibility to calculate the surface energy of a droplet by subtracting the bulk volume contribution from the ground-state energies $E_0^{(0)}(N)$. The usual way for calculating the surface energy of the bulk (see, e.g., Ref. 66) can be used to define the static surface tension of the droplet as

$$\sigma_{stat}(N) = \frac{E_0^{(0)}(N) - \mu_b N}{4\pi R_{eff}^2(N)},\tag{33}$$

where μ_b is the bulk chemical potential ($\mu_b = -7.196$ K at T=0) and R_{eff} is an effective radius of the droplet. The numerator is the difference between the ground-state energy of a droplet $E_0^{(0)}(N)$ and the energy of the same number of atoms in the bulk $\mu_b N$. In the limit $N \rightarrow \infty$, Eq. (33) gives indeed the surface tension of the liquid. The optimal choice of R_{eff} in order to take account of the gradual decrease in the density at the surface is a matter of ongoing discussion in the literature.[67] Here the conventional definition is used according to which R_{eff} is the equivalent radius R_0 of a sharp-edged droplet with a uniform density distribution as defined in Eq. (29). This so-called static surface tension is compared with the dynamic surface tension in Fig. 12.

It is indeed gratifying that the surface tensions determined by these two largely independent methods agree so nicely down to sizes of $N \simeq 30$. This good agreement pro-

vides circumstantial evidence in support of our use of Tamura's formula for estimating $\sigma_{dyn}(N)$. This encourages us to argue that our procedure may also be valid for $N \lesssim 30$ as indicated by the good agreement of not one but three levels at $N \simeq 25$, and even good agreement for the $(0,2)$ and $(0,3)$ levels down to the magic number of $N=14$. The larger values for the static surface tension suggest perhaps that the choice of R_{eff} underestimates the true value.

Thus the extensive calculations presented here provide a new approach for determining the surface tension of small droplets which is an ongoing issue.[67,68] The advantage of the new method used here is that it incorporates the size dependence of a series of excited-state levels instead of only the ground-state energy as in the conventional approach Eq. (33). Although Tamura's formula, Eq. (32), also scales with an estimate of R_d, the width of the outer density falloff region is correctly accounted for in the energy-level differences. Hopefully it will be possible to further improve the liquid-drop model to account for the size dependence of the surface tension in a more rigorous way. An even more microscopic approach can now be envisaged since the pair distribution functions are also available from the DMC calculations.

B. Compressional modes

The liquid-drop model also predicts the existence, for each angular momentum state L, of compressional or breathing modes, which correspond to our vibrational $(n>0,L)$ states. The lowest excitation for $L=0$ has a radial frequency given by[60]

$$\omega_0 = \frac{\pi}{R_0}\left(\frac{b_c}{m}\right)^{1/2},\tag{34}$$

where R_0 is the equivalent uniform droplet radius [Eq. (29)], and b_c is the bulk compressibility coefficient. It is related to the speed of sound c by $b_c = mc^2$ and its bulk value is about 27 K.

The previous discussion about the surface tension suggests a similar analysis of the compressibility coefficient $b_c(N)$ of each cluster. Following the study about the nuclear giant monopolar resonance,[32] the following expression can be deduced from our calculated monopolar excitation energies $\Delta E_0^*(N)$:

$$b_c(N) = \frac{m}{\hbar^2 \pi^2}[\Delta E_0^*(N)R_{eff}(N)]^2.\tag{35}$$

The results are plotted in Fig. 13 (left panel) as dots, together with the bulk compressibility coefficient. In this range of N, the values of the cluster compressibilities are much smaller than in the bulk by a factor of 3.6 at $N=50$. In Fig. 13 (right panel) the energy per particle in the clusters is found to show a remarkably similar trend with the number of constituents, although they are smaller by only about a factor of 2.5 at $N=50$.

VII. CONCLUSIONS

Stimulated by the unexpected observation of magic-enhanced intensities for certain ^{4}He cluster sizes in free jet
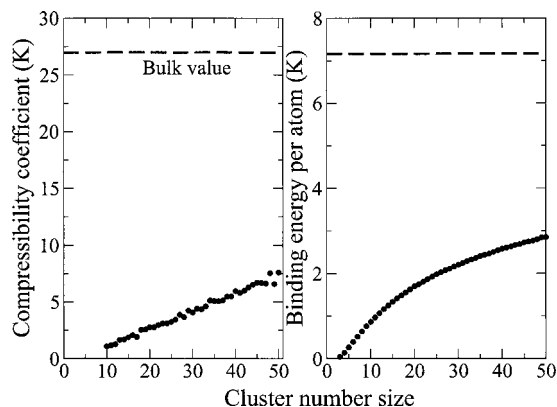
FIG. 13. Left panel: the compressibility coefficient deduced form Eq. (35) as a function of the number N of atoms. Right panel: the energy per particle as a function of the number N of atoms. For comparison, the bulk values are also plotted.

expansions a renewed computational study using the diffusion Monte Carlo 0 K method has been undertaken. The experiments were made possible using matter-wave diffraction from nanostructured transmission gratings, which is provided for a nondestructive analysis of the neutral cluster sizes produced in free jet expansions. In view of the high resolution of the experiments the calculations were carried for each cluster size between $N=3$ and 50 for the first time. Even at this resolution the calculated total ground-state energies show a completely smooth monotonic increase with cluster size. The chemical potential obtained from the slope of the binding energy with size also shows a smooth increase in excellent agreement with earlier calculations for selected sizes[13] and more recent calculations[40] also designed to explain the same experiments. Thus these calculations rule out convincingly the usual explanation of magic numbers in terms of enhanced stabilities for certain cluster sizes. This, perhaps, is not surprising, since the earlier computational studies also did not find enhanced stabilities, which are also not expected *a priori* in view of the liquid nature of the clusters.

Excited-state energy levels were also calculated as a function of N using an importance-sampling technique which is described in detail. For the lowest $n=0$ vibrational mode bound excited states were found for $L=2$, 3, 4, and 5. The size thresholds for binding increased with increasing L. Once bound the level energies decrease slowly with size. They are much smaller than those predicted using the standard liquid-drop model which predicts diverging values with decreasing size. At large sizes, on the other hand, the calculations suggest a behavior which extrapolates to that expected for the liquid-drop model. The dipolar excitation, $L=1$, which is forbidden in a simple collective model because of the center-of-mass constraint does not appear to be bound in the region investigated. The calculation of the vibrational (1,0) mode requires the use of sum rules techniques together with a generic monopolar excitation operator. The optimum calculations reveal a threshold for stability at sizes between 6 and 8, close to the threshold for the $n=0, L=2$ state. As opposed to the $(0, L)$ levels the energy of the (1,0) level increases slowly with size but remains stable up to $N=50$ with an energy well below the chemical potential.

To explain the correspondence between the size thresholds and the observed magic numbers an equilibrium model with a fixed sudden freeze temperature is used to predict the relative cluster concentrations. Thus the ratio of the partition functions which enters into the equilibrium constant shows sharp spikes at threshold sizes independent of the assumed sudden freeze temperature. The calculated size thresholds for stability of these modes are in excellent agreement with the magic numbers at about 10, 14, 26, and 44, but do not lie close to another experimental magic number at $N^*=22$. The good agreement between the experimental magic numbers and theoretical stability thresholds thus provide rather direct confirmation of the theoretical calculations. Furthermore the agreement lends additional credence to the simple sudden freeze equilibrium model of cluster growth.

The theoretical results on the cluster radial distribution functions have been found to be instrumental in understanding the large discrepancies between the energy levels calculated here and those predicted by the liquid-drop model. Using a theory of Tamura[64] part of the differences can be accounted for by the finite width of the radial density at the surface of the clusters. The remaining differences can be largely removed by assuming a smooth decrease in the cluster surface tension with decreasing N. Thus it has been possible to extract for the first time information on the size dependence of the surface tension of small liquid clusters.

Additional insight into the remarkable properties of small ^{4}He clusters comes from the pair distribution functions which are sharply peaked at interparticle distances of about 3.6 Å and pass through a maximum at $N \approx 20$, which is three times larger than in the bulk. Finally a remarkable reduction in the cluster compressibility compared to the bulk could be established.

The present combined theoretical and experimental investigation, we believe, provides the most comprehensive and accurate description of many of the important properties of small ^{4}He clusters. More work remains to be done, for one additional experiment is needed to confirm the magic number $N^*=22$, which cannot be explained presently. Since the concept of temperatures of small clusters is still a somewhat open issue a more realistic model of cluster growth is called for. Also the rate of evaporation from small clusters has so far not been investigated using a microscopic calculation, but is required to estimate the effective temperatures of small clusters. Calculations at finite temperatures would be desirable and indeed it is surprising that few calculations at finite temperatures have been carried out for small ^{4}He clusters.[69–71] Finally the effect of the superfluidity on the physical properties of these small clusters still needs to be examined.

[1] J. P. Toennies and A. F. Vilesov, Angew. Chem., Int. Ed. **43**, 2622 (2004).
[2] See Special Issue on Helium Nanodroplets, J. Chem. Phys. **115**, 10065

(2001).

[3] *Microscopic Approaches to Quantum Liquids in Confined Geometries*, edited by E. Krotscheck and J. Navarro (World Scientific, Singapore, 2002).

[4] M. Barranco, R. Guardiola, E. S. Hernández, R. Mayol, J. Navarro, and M. Pi, J. Low Temp. Phys. **142**, 1 (2006).

[5] J. P. Toennies, *Microscopic Approaches to Quantum Liquids in Confined Geometries* (Ref. 3), Chap. 9, pp. 379–417.

[6] F. Paesani, Y. Kwon, and K. B. Whaley, Phys. Rev. Lett. **94**, 153401 (2005).

[7] V. R. Pandharipande, J. G. Zabolitzky, S. C. Pieper, R. B. Wiringa, and U. Helmbrecht, Phys. Rev. Lett. **50**, 1676 (1983).

[8] S. A. Chin and E. Krotscheck, Phys. Rev. B **45**, 852 (1992).

[9] K. B. Whaley, Int. Rev. Phys. Chem. **13**, 41 (1994).

[10] M. Lewerenz, J. Chem. Phys. **106**, 4596 (1997).

[11] D. M. Ceperley, Rev. Mod. Phys. **67**, 279 (1999).

[12] J. B. Anderson, J. Chem. Phys. **115**, 4546 (2001).

[13] R. Melzer and J. G. Zabolitzky, J. Phys. A **17**, L565 (1984).

[14] J. P. K. Doye and F. Calvo, J. Chem. Phys. **116**, 8307 (2002).

[15] R. Brühl, R. Guardiola, A. Kalinin, O. Kornilov, J. Navarro, T. Savas, and J. P. Toennies, Phys. Rev. Lett. **92**, 185301 (2004).

[16] P. Sindzingre, M. J. Klein, and D. M. Ceperley, Phys. Rev. Lett. **63**, 1601 (1986).

[17] M. Casas and S. Stringari, J. Low Temp. Phys. **79**, 135 (1990).

[18] M. V. Krishna and K. B. Whaley, J. Chem. Phys. **93**, 746 (1990).

[19] R. Guardiola, J. Navarro, and M. Portesi, Phys. Rev. B **63**, 224519 (2001).

[20] M. Hartmann, F. Mielle, J. P. Toennies, A. F. Vilesov, and G. B. Benedek, Phys. Rev. Lett. **76**, 7560 (1996).

[21] S. Grebenev, J. P. Toennies, and A. F. Vilesov, Science **279**, 2083 (1998).

[22] S. Moroni, A. Sarsa, S. Fantoni, K. E. Schmidt, and S. Baroni, Phys. Rev. Lett. **90**, 143401 (2003).

[23] Y. Xu, W. Jäger, J. Tang, and A. R. W. McKellar, Phys. Rev. Lett. **91**, 163401 (2003).

[24] R. A. Aziz, F. R. McCourt, and C. C. K. Wong, Mol. Phys. **61**, 1487 (1987).

[25] R. A. Aziz and M. J. Salman, J. Chem. Phys. **94**, 8047 (1991).

[26] K. T. Tang, J. P. Toennies, and C. L. Yiu, Phys. Rev. Lett. **74**, 1546 (1995).

[27] O. Kornilov, J. P. Toennies, R. Guardiola, and J. Navarro, J. Low Temp. Phys. **138**, 235 (2005).

[28] J. Boronat, *Microscopic Approaches to Quantum Liquids in Confined Geometries* (Ref. 3), Chap. 2, pp. 21–90.

[29] J. Vrbik and S. M. Rothstein, J. Comput. Phys. **63**, 130 (1986).

[30] S. A. Chin, Phys. Rev. A **42**, 6991 (1990).

[31] P. J. Reynolds, D. M. Ceperley, B. J. Alder, and W. A. Lester, Jr., J. Chem. Phys. **77**, 5593 (1982).

[32] O. Bohigas, A. M. Lane, and J. Martorell, Phys. Rep. **51**, 267 (1979).

[33] E. Lipparini and S. Stringari, Phys. Rep. **175**, 103 (1989).

[34] R. P. Feynman and M. Cohen, Phys. Rev. **102**, 1189 (1956).

[35] S. A. Chin and E. Krotscheck, Phys. Rev. Lett. **65**, 2658 (1990).

[36] W. L. McMillan, Phys. Rev. A **138**, 442 (1965).

[37] R. Guardiola, M. Portesi, and J. Navarro, Phys. Rev. B **60**, 6288 (1999).

[38] N. Metropolis, A. W. Rosenbluth, M. N. Rosenbluth, A. H. Teller, and E. W. Teller, J. Chem. Phys. **21**, 1087 (1953).

[39] R. De Bruyn Ouboter and C. N. Yang, Physica B **44**, 127 (1987).

[40] E. Sola, J. Casulleras, and J. Boronat, J. Low Temp. Phys. **134**, 787 (2004).

[41] F. Dalfovo, A. Lastri, L. Pricaupenko, S. Stringari, and J. Treiner, Phys. Rev. B **52**, 1193 (1995).

[42] M. Casas, F. Dalfovo, A. Lastri, Ll. Serra, and S. Stringari, Z. Phys. D: At., Mol. Clusters **35**, 67 (1995).

[43] R. A. Aziz, V. P. S. Nain, J. S. Carley, W. L. Taylor, and G. T. McConville, J. Chem. Phys. **70**, 4330 (1979).

[44] D. Blume and C. H. Greene, J. Chem. Phys. **112**, 8053 (2000).

[45] R. E. Grisenti, W. Schöllkopf, J. P. Toennies, J. R. Manson, T. A. Savas, and H. P. Smith, Phys. Rev. A **61**, 033608 (2000).

[46] W. Schöllkopf and J. P. Toennies, Science **266**, 1345 (1994).

[47] L. Bruch, W. Schöllkopf, and J. P. Toennies, J. Chem. Phys. **117**, 1544 (2002).

[48] R. E. Grisenti, W. Schöllkopf, J. P. Toennies, G. C. Hegerfeldt, and T. Köhler, Phys. Rev. Lett. **83**, 1755 (1999).

[49] F. Bottiglioni, J. Coutant, and M. Fois, Phys. Rev. A **6**, 1830 (1972).

[50] B. E. Callicoatt, K. Förde, L. F. Jung, T. Ruchti, and K. C. Janda, J. Chem. Phys. **109**, 10195 (1998).

[51] A. Kalinin, O. Kornilov, L. Rusin, J. P. Toennies, and G. Vladimirov, Phys. Rev. Lett. **93**, 163402 (2004).

[52] R. M. Villarica, M. J. Casey, J. Goodisman, and J. Chaiken, J. Chem. Phys. **98**, 4610 (1993).

[53] D. R. Miller, in *Atomic and Molecular Beam Methods*, edited by G. Scoles (Oxford University Press, Oxford, 1988), Vol. 1, Chap. 2.

[54] A. Kalinin, O. Kornilov, W. Schöllkopf, and J. P. Toennies, Phys. Rev. Lett. **95**, 113402 (2005).

[55] M. Lewerenz, B. Schillingand, and J. P. Toennies, Chem. Phys. Lett. **206**, 381 (1993).

[56] T. Regge, J. Low Temp. Phys. **9**, 123 (1972).

[57] E. C. Svensson, V. F. Sears, A. D. B. Woods, and P. Martel, Phys. Rev. B **21**, 3638 (1980).

[58] R. E. Grisenti, W. Schöllkopf, J. P. Toennies, G. C. Hegerfeldt, T. Köhler, and M. Stoll, Phys. Rev. Lett. **85**, 2284 (2002).

[59] L. Rayleigh, Proc. R. Soc. London **29**, 71 (1879).

[60] A. Bohr and B. R. Mottelson, *Nuclear Structure*, Nuclear Deformations, II. (World Scientific, Singapore, 1998), pp. 654–676.

[61] S. Stringari, in *The Chemical Physics of Atomic and Molecular Clusters*, edited by G. Scoles (North Holland, Amsterdam, 1990), pp. 223–228.

[62] D. Eichenauer, A. Scheidemann, and J. P. Toennies, Z. Phys. D: At., Mol. Clusters **8**, 295 (1988).

[63] M. Iino, M. Suzuki, and A. J. Ikushima, J. Low Temp. Phys. **61**, 155 (1985).

[64] A. Tamura, Z. Phys. D: At., Mol. Clusters **40**, 225 (1997).

[65] J. Harms, J. P. Toennies, and F. Dalfovo, Phys. Rev. B **58**, 3341 (1998).

[66] J. Treiner and H. Krivine, Ann. Phys. (N.Y.) **170**, 406 (1986).

[67] K. Koga, X. C. Zeng, and A. K. Shchekin, J. Chem. Phys. **109**, 4063 (1998).

[68] A. Laaksonen and R. McGraw, Europhys. Lett. **35**, 367 (1996).

[69] P. Sindzingre, M. L. Klein, and D. M. Ceperley, Phys. Rev. Lett. **63**, 1601 (1989).

[70] A. Guirao, X. Viñas, and M. Pi, Z. Phys. D: At., Mol. Clusters **35**, 199 (1995).

[71] Y. Kwon, D. M. Ceperley, and K. B. Whaley, J. Chem. Phys. **104**, 2341 (1996).